CELLULAR NEUROSCIENCE

The optoretinogram reveals the primary steps of phototransduction in the living human eye

Vimal Prabhu Pandiyan[1], Aiden Maloney-Bertelli[1], James A. Kuchenbecker[1], Kevin C. Boyle[2,3], Tong Ling[2,4], Zhijie Charles Chen[2,3], B. Hyle Park[5], Austin Roorda[6], Daniel Palanker[2,4], Ramkumar Sabesan[1]*

Photoreceptors initiate vision by converting photons to electrical activity. The onset of the phototransduction cascade is marked by the isomerization of photopigments upon light capture. We revealed that the onset of phototransduction is accompanied by a rapid (<5 ms), nanometer-scale electromechanical deformation in individual human cone photoreceptors. Characterizing this biophysical phenomenon associated with photo-transduction in vivo was enabled by high-speed phase-resolved optical coherence tomography in a line-field configuration that allowed sufficient spatiotemporal resolution to visualize the nanometer/millisecond-scale light-induced shape change in photoreceptors. The deformation was explained as the optical manifestation of electrical activity, caused due to rapid charge displacement following isomerization, resulting in changes of electrical potential and surface tension within the photoreceptor disc membranes. These all-optical recordings of light-induced activity in the human retina constitute an optoretinogram and hold remarkable potential to reveal the biophysical correlates of neural activity in health and disease.

INTRODUCTION

Photoreceptors convert light into electrical signals via photo-transduction—a process that has been well-characterized using electrophysiological, pharmacological, and genetic tools (1). Since photoreceptors are the primary cells affected in retinal degeneration, and are the target cells in many treatments (2–4), noninvasive visualization of their physiology at high resolution is invaluable. Full-field and point-scan phase-resolved optical coherence tomography (OCT) (5–7) has been used to image light-induced optical changes in individual photoreceptors with slower temporal signatures (a few seconds) that align with osmotic changes (8) related to the intermediary steps and by-products of phototransduction. These measurements have provided utmost precision in identifying spectral types of cones (7). A population response also showed a fast contraction of the outer segments (≈40 nm in ≈5 ms) immediately following a light flash (5, 7). The mechanism behind the fast contractile response in cone photoreceptors remains poorly characterized and understood largely due to the limited temporal resolution of technologies available for assessing the events that occur at short millisecond time scales.

In general, the physiological processes associated with neural activity affect the cell's refractive index (9) and shape (10, 11), which together alter light propagation, including changes in light scattering (12, 13), polarization (14), and optical path length (OPL) (5). Similarly, cellular deformations accompanying the transmembrane voltage change during action potentials have been documented in crustacean nerves (15), squid giant axons (16), and mammalian neurons (11, 17). Interferometric imaging of these changes, in general, and cellular deformations associated with variations in the cell potential, in particular, offer a noninvasive label-free optical approach to monitor the electrical activity in neurons (10).

The shape of a cell is determined by the balance of the hydrostatic pressure, membrane tension, and stress exerted by its cytoskeleton (18–20). Changes in the membrane potential (i.e., de- or hyper-polarization) alter the repulsive forces between the mobile charges within the Debye layer, thereby affecting the membrane tension. Using atomic force microscopy, Zhang et al. (21) demonstrated that human embryonic kidney (HEK) 293 cells deformed proportionally to the membrane potential change (1 nm per 100 mV). Using quantitative phase microscopy, Ling et al. (10) demonstrated cellular deformations of up to 3 nm during the action potential in spiking HEK293 cells and about 1 nm in mammalian neurons (11). Detecting the millisecond-fast and nanometer-scale cellular deformations in transmission is very challenging because of the OPL difference between the cells and the surrounding medium scales with the refractive index difference, which is only ≈0.02. In contrast to transmission geometry, the corresponding OPL changes when measured in reflection are about 100 times larger since the refractive index difference does not affect it. OPL changes are further compounded in reflection due to the double-pass interaction of light with tissue. However, weak reflection of light from the tissue boundaries limits the backscattered signal, and hence, extracting the nanometer-scale changes from the shot noise remains quite challenging. This challenge is exaggerated in the living retina, where phase stability is severely affected by eye motion. High-speed and precise image registration is required to retrieve weak signals amidst motion due to respiration, heartbeat, and fixational eye movements.

Here, we introduce a high-speed phase-resolved spectral domain OCT in a line-field configuration, which provides sufficient spatio-temporal resolution to facilitate image registration in living eyes and visualize the rapid biophysical changes immediately following light capture in individual cones. We demonstrate the stimulus-induced optical response in cones across varying spatial scales, ranging from hundreds of microns to single cells, without and with adaptive optics (AO). Using high temporal resolutions, ranging

[1]Department of Ophthalmology, University of Washington, Seattle, WA 98109, USA. [2]Hansen Experimental Physics Laboratory, Stanford, CA 94305, USA. [3]Department of Electrical Engineering, Stanford University, Stanford, CA 94305, USA. [4]Department of Ophthalmology, Stanford University, Stanford, CA 94305, USA. [5]Department of Bioengineering, University of California, Riverside, CA 92521, USA. [6]School of Optometry, University of California, Berkeley, CA 94720, USA.
*Corresponding author. Email: rsabesan@uw.edu

from milliseconds to microseconds, and a biophysical model underlying the electromechanical coupling in photoreceptors, we demonstrate that the rapid contractile response of the photoreceptor outer segment is the optical manifestation of electrical activity accompanying photoisomerization, the first steps of phototransduction.

RESULTS

The retina in two cyclopleged subjects was imaged at 5 to 7° temporal eccentricity after 3- to 4-min dark adaptation using a multimodal camera. This included a high-speed line-scan spectral domain OCT for interferometric imaging of cone photoreceptors following light stimulation, a line-scan ophthalmoscope (LSO) for en face imaging of the photoreceptor mosaic and focus optimization, and a 528 ± 20 nm light-emitting diode (LED) source in a Maxwellian view for retinal stimulation (photon density, 10^6 to 10^7 photons/μm^2). Figure 1 describes the experimental paradigm for imaging, stimulation, and analysis (see Materials and Methods for further details). The recorded OCT volumes were reconstructed, registered, and segmented for cone outer segment tips (COST) and inner-outer segment junction (ISOS). The temporal evolution of optical phase difference was computed between the cone ISOS and COST ($\phi_{COST} - \phi_{ISOS}$) to yield a measure of light-induced optical change in the cone outer segments. This response was analyzed for repeatability of magnitude and time course and its dependence on stimulus strength, expressed here as either photon density or percent bleach. Different modes of OCT acquisition and processing—normal or ultrafast, with or without AO, and uniform or patterned stimulation—enabled assessment across a range of spatial and temporal scales. The experimental parameters are summarized in Table 1 (Materials and Methods).

Repeatable biphasic optical change in response to light stimuli in cone photoreceptors

Spatially patterned light stimuli induce consistent patterned responses, encoded in the phase of the OCT signal detected in the outer retina (Fig. 2, A to C). Figure 2A shows an LSO cone photoreceptor image of the retina at 7° temporal eccentricity without AO, overlaid with a spatially patterned illumination (stimulus wavelength, 528 ± 20 nm) of three horizontal bars drawn to scale. Figure 2 (B and C) shows the en face change in OPL between COST and ISOS before ($t = -0.29$ s) and after ($t = 1.05$ s) the stimulus onset, obtained from the OCT phase difference at the two layers, using the relation $\Delta OPL = (\lambda_o/4\pi) \times (\phi_{COST} - \phi_{ISOS})$, where $\lambda_o = 840$ nm. Before the stimulus onset, the phase difference image predominantly denotes the noise floor of the measurement dominated by shot noise but might also include weak responses due to the imaging light itself activating cone photoreceptors. After stimulus onset, the spatial distribution of OPL changes reflects the spatially patterned illumination, reaching an amplitude of 200 nm in ≈1 s. Note, however, that the pattern edges are blurred, potentially due to uncorrected aberrations in the stimulus beam introduced through a dilated pupil. Overall, light-activated responses in the cone outer segments have reliable spatial correspondence with the stimulus patterns on the retina.

An LSO cone photoreceptor image of the retina at 7° temporal eccentricity taken without AO, overlaid with rectangular stimulus areas ranging from 0.06 to 0.27^{o2} is shown in Fig. 2D. Six single OPL recordings (gray dashed lines) after the light onset and their mean (solid line) obtained after averaging phase differences over 0.27^{o2} (yellow rectangle in Fig. 2D) are shown in Fig. 2E. Throughout the ar-

ticle, we will refer to each ΔOPL trace as an optoretinogram (ORG) and, more generally, the optical imaging of stimulus-induced activity as optoretinography. As shown in Fig. 2E, the magnitude and shape of the ORG were very repeatable across trials; the average variability with and without the stimulus was 8 and 2.6 nm, respectively. The photoreceptors exhibited an exceptionally reproducible light-driven response: a rapid (<5 ms) reduction in OPL after the stimulus onset, followed by a slower (>1 s) increase. On the basis of latency with respect to the stimulus onset, we defined the reduction and increase in OPL as the "early" and "late" ORG responses, respectively.

For uncorrelated noise, averaging N samples in space or time improves the signal-to-noise ratio by $1/\sqrt{N}$. The effect of spatial averaging on the light-activated responses was assessed by determining whether phase differences can be averaged over a small retinal area and still demonstrate reasonable fidelity. Figure 2F shows single OPL traces after the light onset averaged over the areas shown in Fig. 2D, demonstrating good consistency in response magnitude and time course for areas as small as 10 cones. The results in Fig. 2F represent only single OPL traces; averaging responses from repeated measurements ought to further improve the signal-to-noise ratio. Results shown in Fig. 2 (A to F) were obtained with optimized defocus but without AO.

Next, we focused on the early contraction that has a lower amplitude and faster temporal signature and assessed whether this phenomenon can be reliably resolved on spatial scales as small as individual cones. For this purpose, AO was incorporated to improve lateral resolution and visualize the en face cone outer segments (Fig. 2G). Figure 2H shows the light-induced (stimulus wavelength, 528 ± 20 nm) OPL changes for a subset of cones in Fig. 2G. Most of the cones in Fig. 2G exhibited the early and late responses, with their respective OPL amplitudes differing substantially. The magnified view immediately after stimulus onset shows an absence of the early response in a subset of cones, constituting putative S-cones. The total differential response amplitude (L/M cones, 347.9 ± 58.4 nm; S-cones, 62.9 ± 25.5 nm) is attributed to a ~100× higher bleach in L/M cones (29.7%) compared to S-cones (0.3%) at the stimulus wavelength centered at 528 nm. Across the 233 and 185 cones tested in subjects 1 and 2, the mean ± SD of the early response amplitude was 42.0 ± 10.8 and 40.8 ± 14.6 nm, respectively. The early and late response amplitudes for each cone are plotted in Fig. 2I. A histogram of the Euclidean distance from the origin denoted the total ORG response amplitude and was subjected to Gaussian mixture model clustering analysis (Fig. 2J) to distinguish the putative S-cones (4.3% of total cones) from L- and M-cones. The S cone density is comparable to in vivo human imaging studies (7, 22–24) (range, 4.2 to 7.7%) and histology (25) (~7%). The response magnitudes were similar for individual cones with AO and for averages obtained under uniform illumination without AO.

Stimulus strength dependence of the early and late cone response

The family of OPL traces (Fig. 3) with increasing stimulus strength, expressed in photon density (photons per square micrometer) and percent bleach for a stimulus wavelength of 528 ± 20 nm, shows that the amplitude of both the late and early responses increases with the stimulus photon density [0.1 × 10^6 to 6 × 10^6 photons/μm^2 for late response (Fig. 3A); 0.04 × 10^6 to 2 × 10^6 photons/μm^2 for early response (Fig. 3D)]. The maximum amplitude of the late response
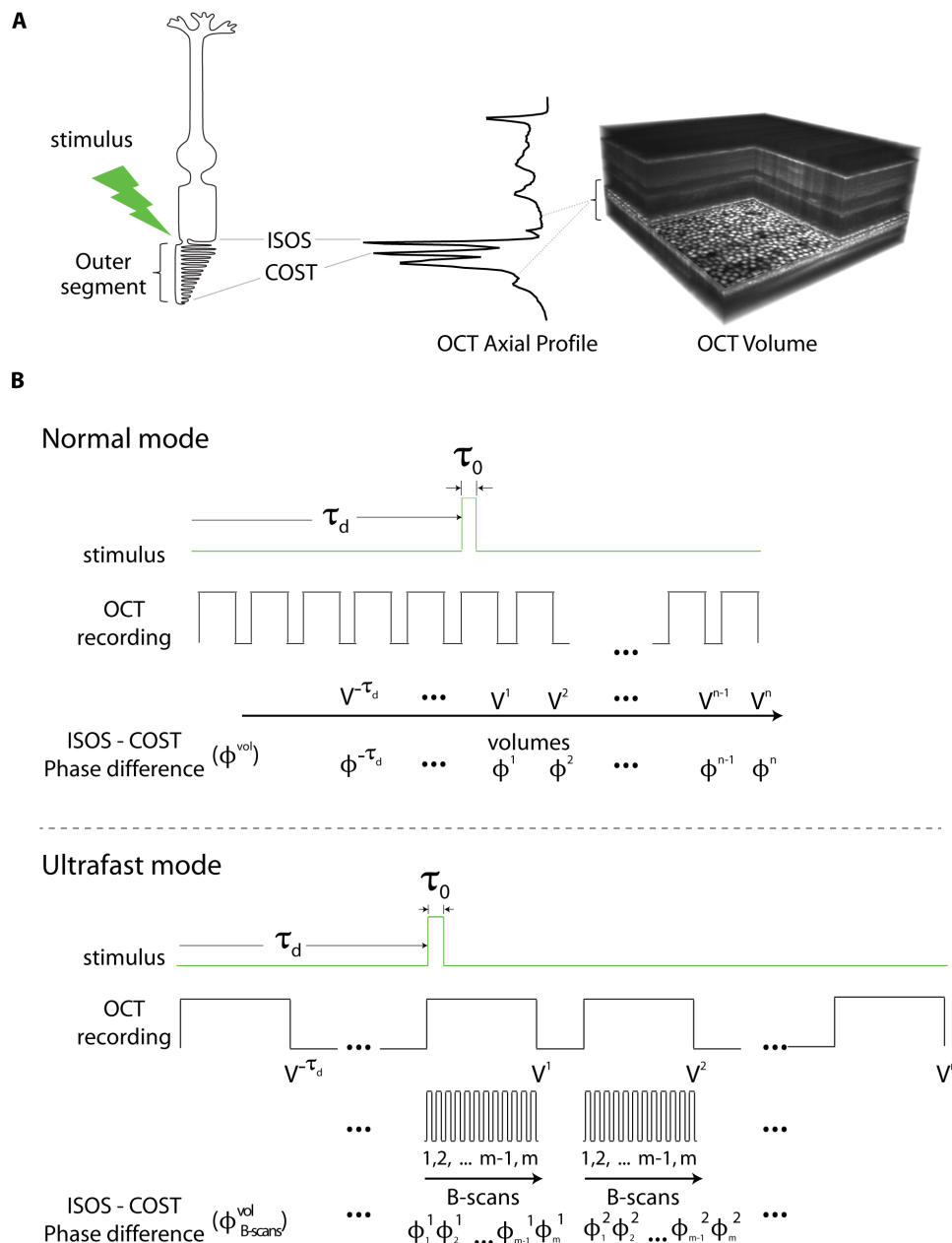
Fig. 1. Optoretinography experimental paradigm. (**A**) High-resolution volumetric imaging using an a line-scan retinal camera. Human retina was visualized using a multimodal camera consisting of fast volumetric imaging with line scan OCT, en face LSO imaging, and a light stimulus in Maxwellian view. A three-dimensional (3D) OCT volume with AO allows resolving the cone mosaic in an en face projection and the outer retinal layers in an axial profile corresponding to the ISOS and COST. Stimulus (528 ± 20 nm, green)–driven changes in a cone photoreceptor are accessible by computing the time-varying phase difference between the proximal and distal OCT reflections encasing the outer segment. (**B**) Modes of acquisition and processing. In both normal and ultrafast modes, a stimulus with pulse width (τ_o) and delay (τ_d) relative to the start of OCT recording illuminated the retina. The OCT volumes (V) were referenced in time to the stimulus onset and ranged from $V^{-\tau_d}$ to V^n. In the normal mode, the phase difference between ISOS and COST was computed for each volume (ϕ^{vol}) and converted to OPL to represent the optical change in cone outer segments following light stimulation. The volume rate (120 to 324 Hz) defined the temporal resolution of the response in the normal mode. In the ultrafast mode, the phase difference was computed for each B-scan within a volume (ϕ_{B-scan}^{vol}) and the B-scan rate (16 kHz) defined the temporal resolution.

versus photon density fits a power function with exponents of 0.5 and 0.6 for subjects 1 and 2, respectively (Fig. 3B), growing from 50 to 527 nm. With increasing photon density, the magnitude of the early response increased from 5 to 57 nm (Fig. 3D). The amplitude of the early response scaled with the stimulus photon density according to a logarithmic function for both the subjects, as shown in Fig. 3E.

To obtain insight into the rapid initiation of the response and time to peak after the stimulus onset, we undertook a modified analysis paradigm that yielded a temporal resolution of 125 μs (see Materials and Methods). Figure 3F shows the early response at high temporal resolution for two photon densities. The latency of the early response onset and time to peak were obtained from bilinear
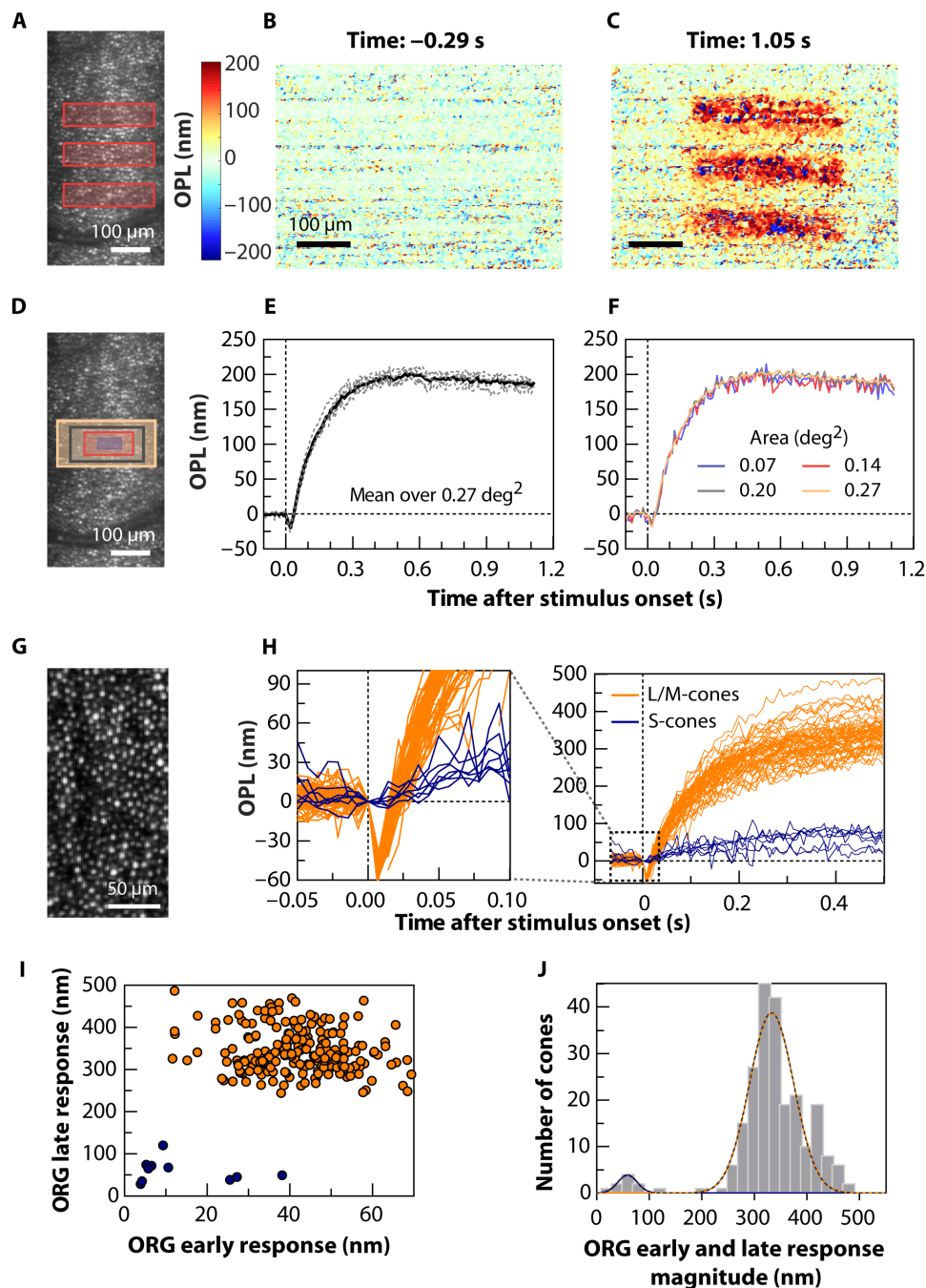
Fig. 2. Optoretinography reveals functional activity in cone outer segments across different spatial scales. (**A**) Illumination pattern (three bars) drawn to scale over the LSO image. (**B** and **C**) The spatial map of OPL change between the ISOS and COST before (B) and after stimulus (C), measured at 20-Hz volume rate. (**D**) Rectangles over an LSO image represent the areas over which averages were obtained to plot the ORGs: $0.27^{\circ 2}$ (yellow), $0.20^{\circ 2}$ (gray), $0.14^{\circ 2}$ (red), and $0.07^{\circ 2}$ encompassing ≈10 cones (violet). (**E**) Repeatability of the response: single ORGs (gray, dashed) and their mean (solid black) for six repeat trials, where phase responses were averaged over $0.27^{\circ 2}$ for 17.9% bleach. (**F**) Spatial averaging: ORGs over different areas color-coded according to the rectangles in (D). (**G**) Maximum intensity projection at COST layer with AO-OCT reveals individual cone photoreceptors. (**H**) ORGs for a subset of single cones in (G) demonstrating the response in each cone for 0.3% S- cone bleach and 29.7% average L and M cone bleach. The magnified view near stimulus onset shows a negligible early response in putative S-cones (blue) compared to L/M cones (orange). (**I**) ORG early and late response amplitudes for each cone in (G). (**J**) Histogram of the ORG early and late response magnitude, computed as the Euclidean distance from origin of each data point in (I). The two-component Gaussian mixture model (black dotted line) and its component Gaussians are used to distinguish S-cones (blue fit) from L/M cones (orange fit). The vertical dotted line marks $t = 0$ in (E), (F), and (H), indicating the rising edge of stimulus onset. (A) to (F) are obtained without AO, with 4-mm imaging pupil, at 120-Hz volume rate. (G) and (H) are obtained with AO, for 6-mm imaging pupil, at 162-Hz volume rate. The stimulus wavelength for all plots is 528 ± 20 nm.
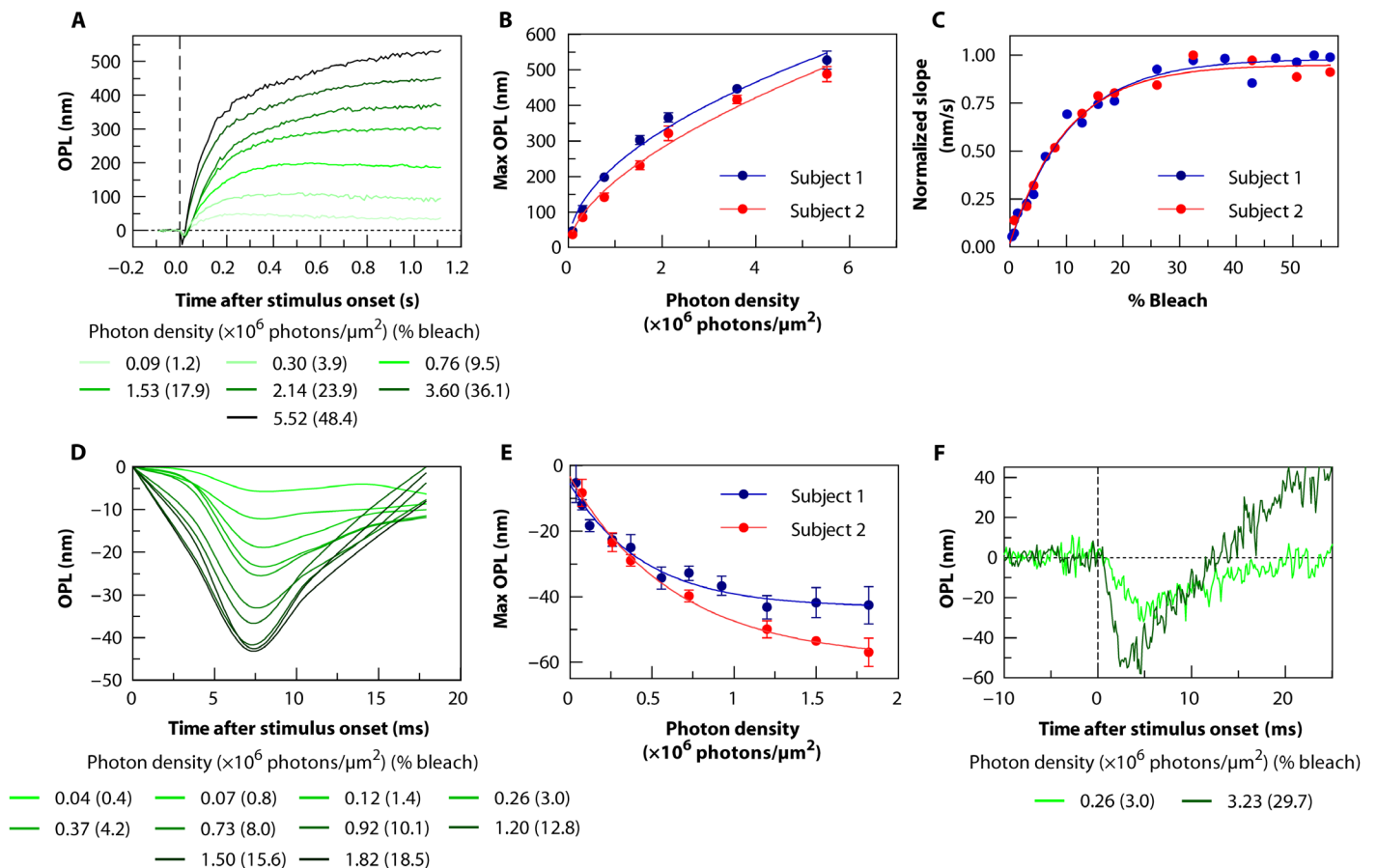
Fig. 3. Stimulus strength dependence of the ORG. (**A**) The early and late response components of the ORG are shown as a function of stimulus strength, expressed here as photon density (photons per square micrometer) and bleach percent. A magnified view of the early response at higher temporal resolution is plotted in (**D**). The maximum OPL change in the late and early responses are shown in (**B**) and (**E**), respectively, with their corresponding best fits (solid line in blue and red) for two subjects. Four individual measurements were averaged for all data shown here in (A) and (D), and error bars denote ±1 SD from the mean. OPL changes are averaged spatially over 0.27°². (**C**) shows the slope of the swelling in the late response for two subjects and its best fit. (**F**) Early response recorded at a high temporal resolution reveals that the onset latency is minimal with respect to the flash onset. Eight individual measurements are averaged in (F). The vertical dotted marks $t = 0$ in (A) and (F) indicate the rising edge of stimulus flash. All data in these figures were collected without AO and with a 4-mm pupil. Volume rates for (A) and (B) is 120 Hz, (C) to (E) is 324 Hz, and (F) is 32 Hz. The stimulus wavelength for all plots is 528 ± 20 nm.

fits to the data (see the Supplementary Materials) and estimated to be 0.21 ms [90% confidence interval (CI), 0 to 0.56] and 4.38 ms (CI, 3.91 to 4.76) for 3.0% bleach and 0.38 ms (90% CI, 0.21 to 0.51) and 2.54 ms (CI, 2.43 to 2.63) for 29.7% bleach.

We interpret the increase in the OPL at slow temporal scales (the late response) to be a result of the diffusion of water into the outer segment to maintain osmotic balance during the phototransduction cascade. This was proposed on the basis of observations made in mouse rod outer segments (*8*). On the basis of the observations of Zhang *et al.* that transducin knockout mice do not show similar osmotic swelling, it follows that the dominant osmolyte implicated in the process must include transducin or its downstream activation stages in the rod phototranduction cascade. Here, in human cones, we find that osmotic equilibrium is reached considerably faster than rods. For example, at 7.5% bleach, cone outer segments equilibrated in ≈300 ms, while for 10% bleach, rod osmotic equilibrium takes over 100 s (*8*). This could partially be explained by the larger membrane surface area in direct contact

with the cytosol in cone outer segment disks, providing a higher effective osmotic permeability. Rod outer segment disks, on the other hand, are disconnected from the plasma membrane and each other. The difference in the time scales of osmotic equilibrium might additionally arise due the kinetic differences in phototransduction between rods and cones (*26*). We sought to examine the faster osmotic equilibrium in cones by characterizing the initial slope of the late response with respect to bleach strength. The rate of increase in OPL within 20 ms following the early response peak is plotted as a function of increasing bleach in Fig. 3C. Following Zhang *et al.* (*8*), the rate of swelling denotes the rate of water entry into the cone outer segments, posited to saturate when phototransduction produces the maximum osmotic stimulus. For future work aimed at determining the responsible osmolytes, it is instructive to note that the 1/e or 63% of slope saturation is achieved with ≈15% bleach of the cone opsins. For subjects 1 and 2, the saturated slope was 4.6 microns per second and 3.9 microns per second, respectively.

Mechanism of cone outer segment contraction

A few key features of the fast contractile response provide insight into its mechanistic origin: The latency of the response was short (sub-millisecond), it peaked earlier with more intense stimuli, the required photon density was high (sufficient to bleach cone photopigments), and the maximum amplitude saturated logarithmically with increasing photon density. These short microsecond-scale latencies are typically not associated with the activation stages of phototransduction, even at high stimulus strength, where, typically, a few millisecond elapses between the stimulus onset and initiation of the cascade (27). Rather, these characteristics of the early response agree well with the early receptor potential (ERP)—a fast electrical signal observed in cone photoreceptors via patch clamp recordings ex vivo under intense flash stimuli (27–29). The ERP is attributed to the charge transfer across the cell membrane associated with the conformational change of opsins embedded in the membrane (30) and is distinct from the later changes in the cell potential due to the closing of ion channels following phototransduction.

Previous observations of the cellular deformations due to changes in the transmembrane potential (10, 21, 31) established a linear relationship between the membrane displacement and cell potential. These are linked by the dependence of the membrane tension on transmembrane voltage (fig. S1B), originating from lateral repulsion of the mobile ions in the Debye layer. The fast hyperpolarization of the disk membrane due to charge transfer associated with conformational changes in opsins during isomerization increases the repulsive forces between charges on the membrane surface, causing the disk membrane to stretch. The individual disks are only open to the rest of the outer segment at the ciliary axoneme (32), as shown in the full cross section in the bottom panel of Fig. 4A. However, the small size of the opening and the large aspect ratio of the disk result in conservation of the cell volume during the millisecond-short events, such that expansion of the disks leads to their flattening, schematically depicted in the top panel of Fig. 4A where the cross section was taken through the width of the disk. We established a theoretical model that combines the dynamics of the ERP, the voltage-dependent membrane tension, and the mechanics of the folded lipid membrane to describe the contraction of the cone outer segments. Here, we outline the key components of the model. A more detailed elaboration of the model appears in a companion article (33).

The membrane area expansion coefficient increases with tension as a result of flattening the thermally induced fluctuations (34). As the membrane stretches, its undulations are reduced, and the membrane becomes more resistant to further deformation, as illustrated in fig. S1B. In a linear approximation of the membrane stiffness scaling with the applied force, the area expansion of the disk $\Delta A/A$ increases logarithmically with the tension (34) $\tilde{\tau}$

$$\frac{\Delta A}{A_0} = \frac{\tilde{\tau}}{K_A} + \frac{k_B T}{8\pi k_c}\ln\left(\frac{\tilde{\tau}A/\pi^2 k_c + 1}{\tilde{\tau}a_1/\pi^2 k_c + 1}\right) \quad (1)$$

where A is the size of the membrane patch (in this case, the area of the photoreceptor disk face), A_0 is the area at zero observable tension $\tilde{\tau}$, a_1 is the smallest bending feature size (area of a lipid head in a simple lipid bilayer membrane), k_B is the Boltzmann constant, T is the temperature, and k_c is the bending modulus. In the case of a membrane densely filled with photopigment molecules (typically making up 50% of the membrane area), a_1 is likely not limited by the lipid head width but rather by the characteristic size of the opsin nanodomains embedded in the disk membrane (35). With a fixed volume in the disk, the change in thickness of the disk $\Delta z/z$ to accommodate this area expansion is

$$\frac{\Delta z}{z} = -\frac{\Delta A}{A} \quad (2)$$

Considering the double pass of light reflected at the bottom of the outer segment, the corresponding change of the OPL in one outer segment disk of height h and refractive index n is

$$\Delta OPL = \frac{\Delta z}{z} \times 2 \times h \times n \quad (3)$$

With light intensities well below saturation (<18.5% bleaching of the opsins), the membrane potential change in the disks does not exceed 2 mV and scales approximately linearly with the number of photons. This corresponds to about 1/100th nanometer OPL decrease per disk, but in an outer segment of ≈30 μm in height, made up of a stack of hundreds of disks, the overall deformation approaches 40 nm (Fig. 4).

The logarithmic relation between the area expansion and membrane tension in Eq. 1: $x \cong \ln(1 + F(x))$ implies an exponential
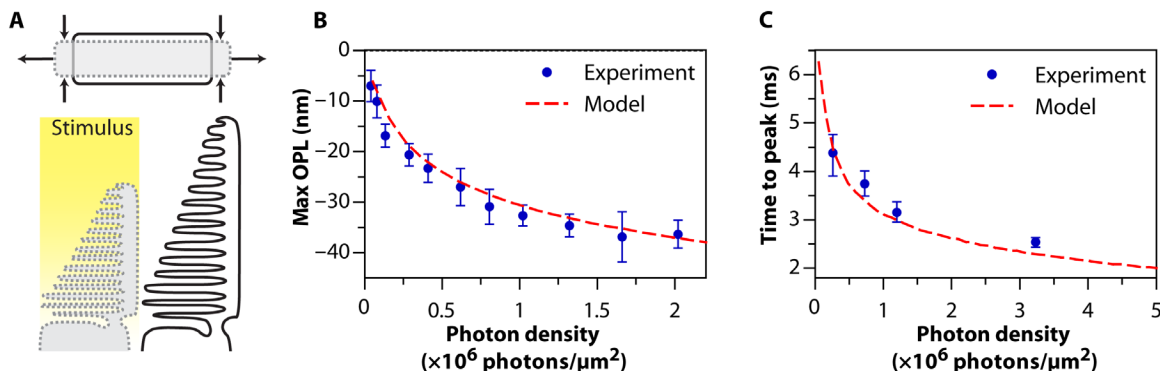

Fig. 4. Mechanism of cone outer segment contraction. (**A**) Repulsion of charges in the hyperpolarized disc membrane leads to its expansion, which results in flattening of the disks due to volume conservation. The illustrations of the cone outer segments shown are not to scale. (**B**) Logarithmic model fit to the maximum amplitude of the early response shown in Fig. 3E. (**C**) Model fit to the time to peak of the early response.

restoring force $F(x) \cong e^{kx} - 1$. By adding a viscous damping term $c\dot{x}$, we arrive at a nondimensionalized equation of motion with four parameters

$$m\ddot{x} + c\dot{x} + (e^{kx} - 1) = F(\text{photons}) = \tau(\text{photons})*l \quad (4)$$

This phenomenological model is fit (determining the parameters m, c, k, and l; see the Supplementary Materials) to two stimulus intensities and yields a very good match to two significant features of the ORG early response in independent measurements. First, the model matches the logarithmic saturation of the amplitude with increasing photon density, as shown in Fig. 4B. Second, it matches the time course of the deformation at different photon density, specifically the earlier time to peak at higher photon density, as shown in Fig. 4C (also see Fig. 3F and fig. S2). The agreement of the model with the experimental results, being consistent in peak deformation and timing across all stimulus strengths with a single set of model parameters (m, c, k, and l), indicates that contraction of the outer segment is indeed driven by the charge transfer across the membrane during ERP. A more detailed description of the model linking the underlying biophysical properties of the membrane to these phenomenological parameters is described elsewhere (33).

DISCUSSION

The line-scan protocol used here provides an optimal trade-off between the speed, resolution, and sensitivity for phase-resolved retinal imaging. By losing confocal gating in one dimension (1D), it gains improved phase stability along the same dimension and one less moving part (scanner) in the optical system. Because an entire X-Z image is obtained in a single camera snapshot, high phase stability across the entire imaging field of the B-scan is achieved at high temporal resolution. These factors are central to resolving the fast and minute optical changes (millisecond/nanometer scale) associated with mechanical deformations in individual cones. Using this interferometric imaging, we quantified the earliest stages of the cone phototransduction in the human retina and elaborated the underlying biophysical mechanisms.

The time course of various stages in the phototransduction cascade has been extensively studied. At high stimulus light levels, as used here, that are sufficient to bleach a significant fraction of the cone opsins ($\approx 10^5$ to 10^7 total photoisomerizations per cone), electrophysiological recordings in primate cone photoreceptors are rare. At bright-light exposures in rods, the G-protein complex is known to disassociate from the disk membrane and translocate (36). Zhang et al. (8) proposed that this causes an osmotic imbalance, leading to water uptake into the outer segment. However, G-proteins, specifically, transducin alone could account only for about 1/10th of the entire magnitude of the outer segment swelling in mouse rods, and hence, other yet unknown mechanisms or osmolytes might be involved as well. In cones, however, given how transducin does not translocate (37), it is unlikely to contribute to the swelling, unless disassociation of the complex from the discs was followed by a fast re-association without translocation. The latter phenomenon though has not previously been described. We find that cones differ markedly in their outer segment swelling response to light stimuli, most significantly, in the amplitude and rate of saturation. However, the characteristics of the late response demand further study to conclusively determine

the osmolytes responsible for the effect. Light flashes that bleach several percent of photopigment elicit a similar rate of increase in photocurrent in both rods and cones, consistent with the idea that the rates of activation in early stages of phototransduction—transducin and phosphodiesterase activation—are very similar between rods and cones (27, 38). Therefore, a model of osmotic swelling would need to account for the differences in permeability, outer segment structure, and later stages of phototransduction to potentially explain the difference between the swelling magnitude, rate, and saturation in rod and cone ORGs.

We observed that the point of inflection, where the early response peaks and the late response initiates, is reached faster at higher stimulus strength by ≈ 1.7 ms between 3.0 and 29.7% bleach (Figs. 3F and 4C). More generally, the rate of change increases with brighter stimuli, i.e., the outer segments undergo a more rapid mechanical deformation, followed by a faster osmotic swelling, compared to that at lower stimulus strength (Fig. 3, D and F). This is analogous to cone photocurrents measured in vitro, where with brighter stimuli, both the cone photocurrent amplitude and the initial rate increase and then eventually saturate when 1 to 2% of pigment is bleached (27). For the same bleach level, Hestrin and Korenbrot (27) also measured a limiting delay for initiation of the cone photocurrent of ≈ 8 ms after the stimulus onset in salamander retina, substantially longer than the onset of the late response here. Note that much shorter latency (up to 3 ms) has been observed in cone-mediated human electroretinography (ERG) a-waves (39), consistent with the latency of the ORG late response observed here: 2.5 ms at 29.7% bleach. Overall, the latency of the initiation of the ORG late response is on a comparable time scale to the onset of cone electrical activity measured in ERGs, although drawing stronger parallels between the temporal features of ORG late response and ERG is reliant on revealing the mechanistic basis of the phototransduction steps implicated in the late response.

The sub-millisecond time scale of the early photoreceptor response is too fast to be affected by the slow osmotic swelling, as the time constant for neuronal swelling is on the order of seconds (40). It is not likely to be explained by changes of the index of refraction either. Variation in the refractive index due to a conformational change of the cone photopigments upon their isomerization can be estimated using the Kramers-Kronig relation (41)

$$n(\omega) = n(\omega_0) + \frac{c}{\pi}\left(\omega^2 - \omega_0^2\right)P\int_0^\infty \frac{\alpha(\omega')}{(\omega^2 - \omega'^2)(\omega_0^2 - \omega'^2)}d\omega' \quad (5)$$

where n is the refractive index, c is the speed of light in vacuum, and $\alpha(\omega)$ is the absorption coefficient at the angular frequency of ω. On the basis of the absorption spectrum shift of rhodopsin upon isomerization (42), the change in the refractive index at the OCT wavelength (840 nm) would be positive and on the order of 10^{-5}, as also measured by Kaplan (43). This cannot explain the negative change of the OPL in the outer segments by about 10^{-3} during the early response observed here.

The electromechanical deformations of about 40 nm in the outer segments of photoreceptors are much larger than those observed in neurons during an action potential (<2 nm), although the voltage swing in photoreceptors is much smaller (<10 mV) than during an action potential (≈ 100 mV). This difference is due to the much softer membranes of the disks and their large number (≈ 1000) in the cone

outer segments. The disk membranes in photoreceptor outer segments have very low tension since they are formed via a blebbing process and contain no actin cortex (44). This allows even the slight 2-mV transmembrane potential they experience at 18.5% bleach to yield a ≈0.04-nm deformation on each disk. These minute mechanical changes add up to a very large deformation, proportional mainly to the total number of photoisomerizations in an outer segment containing about 1000 disks.

The optical measurement of these light-induced signals in the retina is termed optoretinography, in analogy to classical ERG. ORG terminology was proposed by Mulligan *et al.* (45) in 1994 (although these signals were never detected by them) and adopted first by our group in reference to the phase-resolved OCT imaging of the stimulus-induced functional activity in the retina in 2018 (46). We restrict our focus here to the photoreceptor component of the ORG. The ORG enables all-optical label-free monitoring of photoreceptor physiology in humans and has the potential to be applied to other retinal cell types as well. Compared to ERG, the current gold standard for functional evaluation in the clinic, the ORG offers several significant advantages. First, ORGs do not require corneal electrodes. Second, the spatial resolution (testable patch size) is orders of magnitude smaller and with AO can be as small as a single cell. Third, ORGs are directly anchored to the OCT structural image, making the spatial localization of the test unambiguous. Last, while the ORG benefits from AO, it is not essential, and the ORG can therefore be integrated into conventional OCT imaging systems, enabling not only structural but also functional evaluation of the retina as part of a routine ophthalmic exam. Hence, the ORG has immense potential to serve as an effective biomarker of photoreceptor function that could be used for detecting the earliest manifestations of diseases, their progression, and therapeutic efficacy of treatments.

MATERIALS AND METHODS
Experimental setup
A multimodal AO line-scan imager was constructed in free-space to include three illumination and three detection channels, as shown in Fig. 5. A superluminescent diode (λ_o = 840 nm, $\Delta\lambda$ = 50 nm, and 6.2-μm axial resolution in air M-S-840-B-I-20, Superlum, Ireland)

source was used as illumination for OCT and for the LSO, a 980 ± 10 nm (IPSDD0906, Inphenix, USA) source was used for wavefront sensing, and a 528 ± 20 nm LED in Maxwellian view was used for retinal stimulation. For patterned retinal stimulation, a negative 1951 U.S. Air Force (USAF) resolution test target was placed in the LED light path on an XYZ translational stage and optically conjugated to the retina. The XY translation was used to finely position the three bars of interest in the center of the imaging raster. The bars were oriented parallel to the scan dimension. The subject adjusted the perceptual focus of the bars by adjusting the z translational stage. A maximum imaging field of 2° × 2° was provided by illuminating a line field on the retina using a cylindrical lens (ACY254-100-B, Thorlabs Inc.) and scanning it with a 1D galvo-scanner (6210H, Cambridge Technology, USA) to image volumes. The AO subsystem included a custom Shack-Hartmann wavefront sensor [Lenslet array: MLA150-7AR(-M) (Thorlabs Inc., USA) and charge-coupled device camera: Grasshopper3 GS3-U3-15S5M (FLIR, USA)] and a deformable mirror (Alpao, DM97-15, France) incorporated into the optical path. The eye's pupil, the scanner, and the deformable mirror were optically conjugated using achromatic lens-based afocal telescopes. An artificial pupil was set to 4 and 6 mm for non-AO and AO imaging, respectively, and defocus was optimized using either the deformable mirror or trial lens for non-AO conditions. A lens-based reference arm was used to reduce diffraction due to long-distance beam propagation and compensate dispersion at the same time. In detection, a 1200 line pairs per millimeter diffraction grating and a high-speed 2D camera (pixel size, 20 μm; Photron, FASTCAM Mini Ax200) formed the spectrometer for OCT. The spatial and spectral resolution (512 × 768 pixels) were optimized in detection by an anamorphic configuration, consisting of two positive cylindrical lenses that allowed governing magnification asymmetrically in both dimensions. The B-scan or M-scan rate was decided by the camera frame rate and varied between 3 and 16.2 kHz in this study. The zeroth-order beam of the grating, which is usually discarded in a traditional spectral-domain OCT system, was used to construct an LSO by placing a focusing lens and a line-scan camera. Because the LSO sensor was optically conjugated to the OCT imaging camera, the en face LSO images were also used to optimize the best focus for imaging. Custom-built software was developed in LabVIEW to

Table 1. Summary of stimulus and imaging parameters for optoretinography.

Stimulus parameters					Imaging parameters				
	Pulse width τ_0 (ms)	Delay (τ_d) (vols/B-scans)	Spatial size (deg^2)	Bleach* (%)	Speed (Hz) B-scan/vol rate	Pupil size (mm)	Field of view scan *x* line (°)	No. of vols	No. of repeats
ORG early response	5	20 vols	37.5	0.4 – 18.5	16200/324	4	0.6 × 1.4	162	4
ORG late response	3 – 70	10 vols	37.5	1.2 – 48.4	8400/120	4	0.6 × 1.4	120	4
ORG ultrafast response	5	10 vols and 100 B-scans	37.5	3.0 – 29.7	16000/32	4	1.7 × 1.4	25	8
ORG early and late response with AO	5	10 vols	37.5	29.7	16200/162	6	0.8 × 1.4	80	12

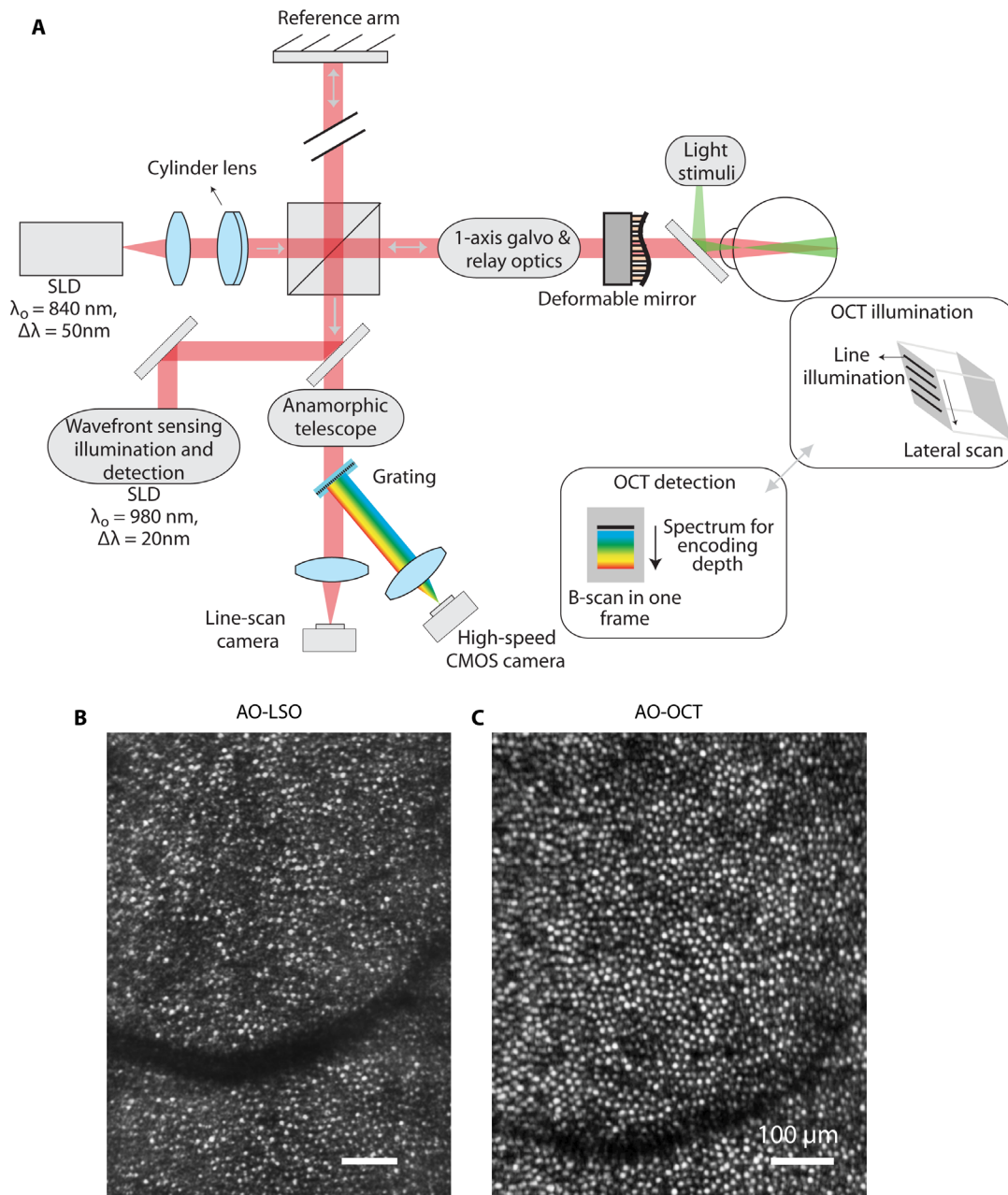*Bleach percent for average of L/M cones. Vols, volumes.

Fig. 5. Optoretinography schematic and representative retinal images. (A) Block diagram of optoretinography system showing key components and features (details in Materials and Methods). AO-LSO (**B**) and AO-OCT images (**C**) of cone photoreceptors at 7° eccentricity. The images are registered and field flattened to compensate for the Gaussian intensity distribution along the line dimension. SLD, Superluminescent diode; CMOS, complementary metal-oxide semiconductor.

synchronize the scanner, frame grabbers, and data acquisition and allowed real-time feedback to the experimenter for subject alignment via live image visualization. The Nyquist-limited lateral resolution of the system was 2.4 µm, system sensitivity was 92 dB, and the phase sensitivity was 4 mrad at a signal-to-noise ratio of 50 dB, where 1 mrad ≈ 0.07 nm for $\lambda_o = 840$ nm. The maximum volume rate used in this study was 324 Hz for 768 × 512 × 50 ($\lambda \times x \times y$) pixels in cases where the temporal resolution of the early response had to be maximized. Further details on optical design, development, and characterization of the instrument are provided elsewhere (*47*).

Optoretinography protocol

Two cyclopleged subjects free of retinal disease participated in the study. Cycloplegia served to arrest accommodative fluctuations for non-AO imaging and dilate the pupil to provide increased numerical aperture and signal-to-noise ratio for AO imaging. It was introduced using Tropicamide 1% ophthalmic solution (Akorn Inc.). The research was approved by the University of Washington institutional review board, and all subjects signed an informed consent before their participation and after the nature and possible consequences of the study were explained. All procedures involving human subjects were in accordance with the tenets of the Declaration of Helsinki.

The subjects were imaged at 5- to 7-° temporal to the fovea. For ORGs, the subjects were dark adapted for 3 to 4 min, and OCT volumes were acquired for 1 to 2 s at different volume rates. After a delay defined by the number of volumes (τ_d), a 528 ± 20 nm LED flash illuminated the retina with pulse width (τ_o). The photon density (photons per square micrometer) illuminating the retina was converted to bleach percentages using published methods (*48*) by accounting for the LED spectral output, the mean of L- and M-cone spectral sensitivity and human cone inner and outer segment geometry. The stimulus and recording parameters are summarized in Table 1 for the different ORG modes of operation. To optimize temporal resolution and reveal details of the early response, lateral resolution and field of view were sacrificed along the scan dimension, such that a minimum of 0.6° × 1.4° (scan × line dimension) was used. To test the performance limits of the system and image the individual cone early responses, a field of view of 0.8° and sparse lateral resolution of 4.6 μm were used to achieve maximum volume rates of 162 Hz. Different numbers of volumes and the number of repeat measurements per condition were acquired. These were chosen as such to optimize the trade-off between capturing relevant features in the ORG response versus the data transfer times from the camera flash memory to the computer. For the ultrafast mode, two B-scans, each taken at 16 kHz, were averaged to obtain a high temporal resolution of 125 μs. Analysis to obtain the latency and peak of the early response from the ultrafast mode is described in Results and Supplementary Text.

Image processing

OCT image processing followed conventional techniques. The acquired OCT data were resampled in *k*-space and Fourier-transformed along the wave number dimension to extract complex-valued retinal volumes. For imaging structure, only the absolute value of the complex number was used. Each OCT volume was segmented, and en face images were obtained by taking the maximum intensity projections centered at the COST for visualizing the cone photoreceptors. En face images were registered using a strip-based registration algorithm and averaged. For optoretinography, the phase analysis followed Hillmann *et al.* (*5*). Each OCT volume was first registered and referenced to the mean of all volumes recorded before the start of stimulus to cancel arbitrary phase noise and set the baseline. From these referenced volumes, a 3-pixel mean of complex values centered at the ISOS and COST was calculated. The phase difference between these two layers was calculated by multiplying the complex conjugate of COST with the ISOS layer and calculating the argument of the resulting product. For strong phase responses that exceed ±π radians, phase was unwrapped along the time dimension at each pixel. The change in OPL was calculated by the relation $\Delta OPL = (\lambda_o/4\pi) \times (\phi_{COST} - \phi_{ISOS})$, where $\lambda_o = 840$ nm.

SUPPLEMENTARY MATERIALS

Supplementary material for this article is available at http://advances.sciencemag.org/cgi/content/full/6/37/eabc1124/DC1

View/request a protocol for this paper from *Bio-protocol*.

REFERENCES AND NOTES

1. V. Y. Arshavsky, T. D. Lamb, E. N. Pugh Jr., G proteins and phototransduction. *Annu. Rev. Physiol.* **64**, 153–187 (2002).
2. D. A. Lamba, J. Gust, T. A. Reh, Transplantation of human embryonic stem cell-derived photoreceptors restores some visual function in Crx-deficient mice. *Cell Stem Cell* **4**, 73–79 (2009).
3. J. Bennett, T. Tanabe, D. Sun, Y. Zeng, H. Kjeldbye, P. Gouras, A. M. Maguire, Photoreceptor cell rescue in retinal degeneration (rd) mice by in vivo gene therapy. *Nat. Med.* **2**, 649–654 (1996).
4. V. Busskamp, J. Duebel, D. Balya, M. Fradot, T. J. Viney, S. Siegert, A. C. Groner, E. Cabuy, V. Forster, M. Seeliger, M. Biel, P. Humphries, M. Paques, S. Mohand-Said, D. Trono, K. Deisseroth, J. A. Sahel, S. Picaud, B. Roska, Genetic reactivation of cone photoreceptors restores visual responses in retinitis pigmentosa. *Science* **329**, 413–417 (2010).
5. D. Hillmann, H. Spahr, C. Pfäffle, H. Sudkamp, G. Franke, G. Hüttmann, In vivo optical imaging of physiological responses to photostimulation in human photoreceptors. *Proc. Natl. Acad. Sci.* **113**, 13138–13143 (2016).
6. M. Azimipour, J. V. Migacz, R. J. Zawadzki, J. S. Werner, R. S. Jonnal, Functional retinal imaging using adaptive optics swept-source OCT at 1.6 MHz. *Optica* **6**, 300–303 (2019).
7. F. Zhang, K. Kurokawa, A. Lassoued, J. A. Crowell, D. T. Miller, Cone photoreceptor classification in the living human eye from photostimulation-induced phase dynamics. *Proc. Natl. Acad. Sci. U.S.A.* **116**, 7951–7956 (2019).
8. P. Zhang, R. J. Zawadzki, M. Goswami, P. T. Nguyen, V. Yarov-Yarovoy, M. E. Burns, E. N. Pugh Jr., In vivo optophysiology reveals that G-protein activation triggers osmotic swelling and increased light scattering of rod photoreceptors. *Proc. Natl. Acad. Sci.* **114**, E2937–E2946 (2017).
9. A. J. Foust, D. M. Rector, Optically teasing apart neural swelling and depolarization. *Neuroscience* **145**, 887–899 (2007).
10. T. Ling, K. C. Boyle, G. Goetz, P. Zhou, Y. Quan, F. S. Alfonso, T. W. Huang, D. Palanker, Full-field interferometric imaging of propagating action potentials. *Light Sci. Appl.* **7**, 107 (2018).
11. T. Ling, K. C. Boyle, V. Zuckerman, T. Flores, C. Ramakrishnan, K. Deisseroth, D. Palanker, High-speed interferometric imaging reveals dynamics of neuronal deformation during the action potential. *Proc. Natl. Acad. Sci.* **117**, 10278–10285 (2020).
12. L. B. Cohen, R. D. Keynes, B. Hille, Light scattering and birefringence changes during nerve activity. *Nature* **218**, 438–441 (1968).
13. R. F. Cooper, W. S. Tuten, A. Dubra, D. H. Brainard, J. I. W. Morgan, Non-invasive assessment of human cone photoreceptor function. *Biomed. Opt. Express* **8**, 5098–5112 (2017).
14. H. Wang, T. Akkin, C. Magnain, R. Wang, J. Dubb, W. J. Kostis, M. A. Yaseen, A. Cramer, S. Sakadzic, D. Boas, Polarization sensitive optical coherence microscopy for brain imaging. *Opt. Lett.* **41**, 2213–2216 (2016).
15. B. C. Hill, E. D. Schubert, M. A. Nokes, R. P. Michelson, Laser interferometer measurement of changes in crayfish axon diameter concurrent with action potential. *Science* **196**, 426–428 (1977).
16. T. Akkin, D. Landowne, A. Sivaprakasam, Optical coherence tomography phase measurement of transient changes in squid giant axons during activity. *J. Membr. Biol.* **231**, 35–46 (2009).
17. Y. Yang, X. W. Liu, H. Wang, H. Yu, Y. Guan, S. Wang, N. Tao, Imaging action potential in single mammalian neurons by tracking the accompanying sub-nanometer mechanical motion. *ACS Nano* **12**, 4186–4193 (2018).
18. K. Keren, Z. Pincus, G. M. Allen, E. L. Barnhart, G. Marriott, A. Mogilner, J. A. Theriot, Mechanism of shape determination in motile cells. *Nature* **453**, 475–480 (2008).
19. N. C. Gauthier, T. A. Masters, M. P. Sheetz, Mechanical feedback between membrane tension and dynamics. *Trends Cell Biol.* **22**, 527–535 (2012).
20. P. Sens, J. Plastino, Membrane tension and cytoskeleton organization in cell motility. *J. Phys. Condens. Matter* **27**, 273103 (2015).
21. P.-C. Zhang, A. M. Keleshian, F. Sachs, Voltage-induced membrane movement. *Nature* **413**, 428–432 (2001).
22. A. Roorda, D. R. Williams, The arrangement of the three cone classes in the living human eye. *Nature* **397**, 520–522 (1999).
23. H. Hofer, J. Carroll, J. Neitz, M. Neitz, D. R. Williams, Organization of the human trichromatic cone mosaic. *J. Neurosci.* **25**, 9669–9679 (2005).
24. R. Sabesan, H. Hofer, A. Roorda, Characterizing the human cone photoreceptor mosaic via dynamic photopigment densitometry. *PLOS ONE* **10**, e0144891 (2015).
25. C. A. Curcio, K. A. Allen, K. R. Sloan, C. L. Lerea, J. B. Hurley, I. B. Klock, A. H. Milam, Distribution and morphology of human cone photoreceptors stained with anti-blue opsin. *J. Comp. Neurol.* **312**, 610–624 (1991).
26. J. I. Korenbrot, Speed, sensitivity, and stability of the light response in rod and cone photoreceptors: Facts and models. *Prog. Retin. Eye Res.* **31**, 442–466 (2012).
27. S. Hestrin, J. Korenbrot, Activation kinetics of retinal cones and rods: Response to intense flashes of light. *J. Neurosci.* **10**, 1967–1973 (1990).
28. K. T. Brown, M. Murakami, A new receptor potential of the monkey retina with no detectable latency. *Nature* **201**, 626–628 (1964).
29. A. L. Hodgkin, P. M. Obryan, Internal recording of the early receptor potential in turtle cones. *J. Physiol.* **267**, 737–766 (1977).

30. C. L. Makino, W. R. Taylor, D. A. Baylor, Rapid charge movements and photosensitivity of visual pigments in salamander rods and cones. *J. Physiol.* **442**, 761–780 (1991).

31. S. Oh, C. Fang-Yen, W. Choi, Z. Yaqoob, D. Fu, Y. Park, R. R. Dassari, M. S. Feld, Label-free imaging of membrane potential using membrane electromotility. *Biophys. J.* **103**, 11–18 (2012).

32. D. Mustafi, A. H. Engel, K. Palczewski, Structure of cone photoreceptors. *Prog. Retin. Eye Res.* **28**, 289–302 (2009).

33. K. C. Boyle, Z. C. Chen, T. Ling, V. P. Pandiyan, J. Kuchenbecker, R. Sabesan, D. Palanker, On mechanisms of light-induced deformations in photoreceptors. *bioRxiv*, 2020.2001.0008.897728 (2020).

34. D. Marsh, Renormalization of the tension and area expansion modulus in fluid membranes. *Biophys. J.* **73**, 865–869 (1997).

35. T. Rakshit, S. Senapati, S. Sinha, A. M. Whited, P. S. Park, Rhodopsin forms nanodomains in rod outer segment disc membranes of the cold-blooded *Xenopus laevis*. *PLOS ONE* **10**, e0141114 (2015).

36. M. Sokolov, A. L. Lyubarsky, K. J. Strissel, A. B. Savchenko, V. I. Govardovskii, E. N. Pugh Jr., V. Y. Arshavsky, Massive light-driven translocation of transducin between the two major compartments of rod cells: A novel mechanism of light adaptation. *Neuron* **34**, 95–106 (2002).

37. E. S. Lobanova, R. Herrmann, S. Finkelstein, B. Reidel, N. P. Skiba, W.-T. Deng, R. Jo, E. R. Weiss, W. W. Hauswirth, V. Y. Arshavsky, Mechanistic basis for the failure of cone transducin to translocate: Why cones are never blinded by light. *J. Neurosci.* **30**, 6815–6824 (2010).

38. W. H. Cobbs, E. N. Pugh Jr., Kinetics and components of the flash photocurrent of isolated retinal rods of the larval salamander, *Ambystoma tigrinum*. *J. Physiol.* **394**, 529–572 (1987).

39. J. van Hateren, T. Lamb, The photocurrent response of human cones is fast and monophasic. *BMC Neurosci.* **7**, 34 (2006).

40. B. Rappaz, P. Marquet, E. Cuche, Y. Emery, C. Depeursinge, P. Magistretti, Measurement of the integral refractive index and dynamic cell morphometry of living cells with digital holographic microscopy. *Opt. Express* **13**, 9361–9373 (2005).

41. W. Song, L. Zhang, S. Ness, J. Yi, Wavelength-dependent optical properties of melanosomes in retinal pigmented epithelium and their changes with melanin bleaching: A numerical study. *Biomed. Opt. Express* **8**, 3966–3980 (2017).

42. T. M. Thaker, A. I. Kaya, A. M. Preininger, H. E. Hamm, T. M. Iverson, Allosteric mechanisms of G protein-coupled receptor signaling: A structural perspective. *Methods Mol. Biol.* **796**, 133–174 (2012).

43. M. W. Kaplan, Modeling the rod outer segment birefringence change correlated with metarhodopsin II formation. *Biophys. J.* **38**, 237–241 (1982).

44. S. Papal, M. Cortese, K. Legendre, N. Sorusch, J. Dragavon, I. Sahly, S. Shorte, U. Wolfrum, C. Petit, A. El-Amraoui, The giant spectrin βV couples the molecular motors to phototransduction and Usher syndrome type I proteins along their trafficking route. *Hum. Mol. Genet.* **22**, 3773–3788 (2013).

45. J. B. Mulligan, D. I. MacLeod, I. C. Statler, *In search of an optoretinogram*. (1994).

46. V. P. Pandiyan, A. M. Bertelli, J. A. Kuchenbecker, B. H. Park, D. V. Palanker, A. Roorda, R. Sabesan, Optoretinogram: Stimulus-induced optical changes in photoreceptors observed with phase-resolved line-scan OCT. *Invest. Ophthalmol. Vis. Sci.* **60**, 1426–1426 (2019).

47. V. P. Pandiyan, X. Jiang, A. M. Bertelli, J. A. Kuchenbecker, U. Sharma, R. Sabesan, High-speed adaptive optics line-scan OCT for cellular-resolution optoretinography. *Biomed. Opt. Express.* **11**, 5274–5296 (2020).

48. P. Zhang, M. Goswami, R. J. Zawadzki, E. N. Pugh Jr., The photosensitivity of rhodopsin bleaching and light-induced increases of fundus reflectance in mice measured in vivo with scanning laser ophthalmoscopy. *Invest. Ophthalmol. Vis. Sci.* **57**, 3650–3664 (2016).

49. A. F. X. Goldberg, O. L. Moritz, D. S. Williams, Molecular basis for photoreceptor outer segment architecture. *Prog. Retin. Eye Res.* **55**, 52–81 (2016).

50. S. Hestrin, Acylation reactions mediated by purified acetylcholine esterase. *Biochim. Biophys. Acta* **4**, 310–321 (1950).

51. R. Phillips, in *Physics of Biological Membranes* P. Bassereau, P. Sens, Eds. (Springer International Publishing, 2018), pp. 73–105.

52. J. R. Dormand, P. J. Prince, A family of embedded Runge-Kutta formulae. *J. Comput. Appl. Math.* **6**, 19–26 (1980).

53. P. Virtanen, R. Gommers, T. E. Oliphant, M. Haberland, T. Reddy, D. Cournapeau, E. Burovski, P. Peterson, W. Weckesser, J. Bright, S. J. van der Walt, M. Brett, J. Wilson, K. J. Millman, N. Mayorov, A. R. J. Nelson, E. Jones, R. Kern, E. Larson, C. J. Carey, İ. Polat, Y. Feng, E. W. Moore, J. V. Plas, D. Laxalde, J. Perktold, R. Cimrman, I. Henriksen, E. A. Quintero, C. R. Harris, A. M. Archibald, A. H. Ribeiro, F. Pedregosa, P. van Mulbregt; SciPy 1.0 Contributors, SciPy 1.0: Fundamental algorithms for scientific computing in Python. *Nat. Methods* **17**, 261–272 (2020).

Science Advances

The optoretinogram reveals the primary steps of phototransduction in the living human eye

Vimal Prabhu Pandiyan, Aiden Maloney-Bertelli, James A. Kuchenbecker, Kevin C. Boyle, Tong Ling, Zhijie Charles Chen, B. Hyle Park, Austin Roorda, Daniel Palanker and Ramkumar Sabesan

ARTICLE TOOLS	http://advances.sciencemag.org/content/6/37/eabc1124
SUPPLEMENTARY MATERIALS	http://advances.sciencemag.org/content/suppl/2020/09/04/6.37.eabc1124.DC1
REFERENCES	This article cites 50 articles, 9 of which you can access for free http://advances.sciencemag.org/content/6/37/eabc1124#BIBL
PERMISSIONS	http://www.sciencemag.org/help/reprints-and-permissions

Use of this article is subject to the Terms of Service